Measurements of long-range enhanced collisional velocity drag through plasma wave damping

M. Affolter,[a)] F. Anderegg, D. H. E. Dubin, and C. F. Driscoll
Department of Physics, University of California at San Diego, La Jolla, California 92093, USA

We present damping measurements of axial plasma waves in magnetized, multispecies ion plasmas. At high temperatures $T \gtrsim 10^{-2}$ eV, collisionless Landau damping dominates, whereas, at lower temperatures $T \lesssim 10^{-2}$ eV, the damping arises from interspecies collisional drag, which is dependent on the plasma composition and scales roughly as $T^{-3/2}$. This drag damping is proportional to the rate of parallel collisional slowing, and is found to exceed classical predictions of collisional drag damping by as much as an order of magnitude, but agrees with a new collision theory that includes long-range collisions. Centrifugal mass separation and collisional locking of the species occur at ultra-low temperatures $T \lesssim 10^{-3}$ eV, which reduce the drag damping from the $T^{-3/2}$ collisional scaling. These mechanisms are investigated by measuring the damping of higher frequency axial modes, and by measuring the damping in plasmas with a non-equilibrium species profile. *Published by AIP Publishing.*
https://doi.org/10.1063/1.5016194

I. INTRODUCTION

In magnetized plasmas, the rate of particle collisions is enhanced over classical predictions when the cyclotron radius r_c is less than the Debye length λ_D. Classical theories[1–3] describe local velocity scattering collisions with impact parameters $\rho < r_c$. However, when $r_c < \lambda_D$, long-range collisions exchange energy and momentum over the range $r_c < \rho < \lambda_D$ with negligible parallel-to-perpendicular velocity scattering. For electrons with density n_e and magnetic field B, the regime $r_c < \lambda_D$ requires $(B/1 \text{ T})^2 > (n_e/10^{13} \text{ cm}^{-3})$, which occurs in the edge region of tokamak plasmas[4–6] and some astrophysical plasmas.[7] Penning trap plasmas for both matter and antimatter[8–10] are also in this magnetized regime. Previous experiments and theory have shown that these long-range collisions enhance cross-field diffusion,[11,12] heat transport,[13,14] and viscosity[15,16] by orders of magnitude over classical theory when $r_c < \lambda_D$.

Recent theory[17] of long-range collisions predicts strongly enhanced parallel drag in magnetized plasmas for which $r_c < \lambda_D$. This theory resolves inconsistencies between Fokker-Planck[18] and Boltzmann[19] analysis on the effect of long-range collisions on frictional drag by identifying a new fundamental length scale $d \sim b(\bar{v}^2/b^2\nu_{ss'}^2)^{1/5} \propto T^{1/5}$ (defined in detail later), which divides these analysis into separate regimes of validity. Here, $b = q_s^2/T$ is the distance of closest approach, $\bar{v}$ is the thermal velocity, and $\nu_{ss'}$ is the collision rate. When $\rho < d$, the colliding particles can be treated as two-body, point-like Boltzmann collisions, whereas, when $\rho > d$, multiple weak collisions occur simultaneously and Fokker-Planck analysis is required. This theory predicts that the rate of collisional slowing parallel to the magnetic field is increased by long-range collisions, with a larger enhancement at higher magnetic fields, lower densities, and lower temperatures.

Here, we present detailed damping measurements of axial plasma waves in magnetized, multispecies ion plasmas. At low temperatures, collisional drag damping dominates over Landau damping, and we measure damping rates dependent on the plasma composition and scaling roughly as $T^{-3/2}$. We show that this drag damping is proportional to the parallel collisional slowing rate, and therefore provides a test of this new long-range collision theory.[17] Measurements are in quantitative agreement with a collisional drag damping theory only when long-range collisions are included,[20] exceeding classical short-range collision predictions by as much as an order of magnitude.

At ultra-low temperatures, the damping is observed to decrease from the $T^{-3/2}$ collisional scaling as the species centrifugally separate radially, and the fluid elements began to collisionally lock. These effects occur at nearly the same temperature $T \lesssim 10^{-3}$ eV. To isolate the effect of centrifugal mass separation, we measure the damping in plasmas with a non-equilibrium species profile. We find that separating the species radially reduces this interspecies drag damping. The effect of fluid locking is investigated through damping measurements of higher frequency axial modes. Stronger damping is observed at these ultra-low temperatures for the higher frequency modes suggesting less fluid locking in qualitative agreement with theory.

II. EXPERIMENTAL APPARATUS

A 3 Tesla Penning-Malmberg trap[21] confines these cylindrical, multispecies ion plasmas as shown in Fig. 1. The plasmas consists mostly of Mg^+ ions with a 5%–30% fraction of impurities, predominantly H_3O^+, resulting from ionization and chemical reactions with the background gas. By changing the background gas pressure over the range $2 \times 10^{-10} \leq P \leq 7 \times 10^{-9}$ Torr, the shot-to-shot fraction of impurity ions is varied.

On the 8-sectored ring shown in Fig. 1, a weak "rotating wall" (RW) perturbation[22] is applied, which confines these
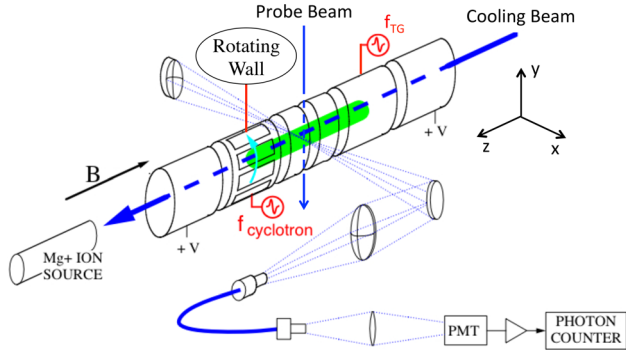

FIG. 1. Schematic of the 3 T Penning-Malmberg trap used to confine and diagnose these multispecies ion plasmas.

ions for days in a near thermal equilibrium state described by "top-hat" density and rigid-rotor rotation profiles. Radial profiles of the total Mg^+ density, rotation velocity, and plasma temperature are measured through Laser Induced Fluorescence (LIF) techniques.[21] A typical plasma has a radius $R_p \sim 0.5$ cm, density $n_0 \sim 1.9 \times 10^7$ cm^{-3}, and length $L_p \sim 10$ cm, and rotates at $f_E \sim 9$ kHz. By changing the frequency of the RW, the rotation rate $f_E = (4 \rightarrow 31)$ kHz and thus the plasma density $n_0 = (0.9 \rightarrow 6.4) \times 10^7$ cm^{-3} are varied.

At high temperatures $T \gtrsim 10^{-3}$ eV, the species are uniformly mixed as shown in the radial density profile of Fig. 2 (Top), whereas, at lower temperatures $T \lesssim 10^{-3}$ eV, the species
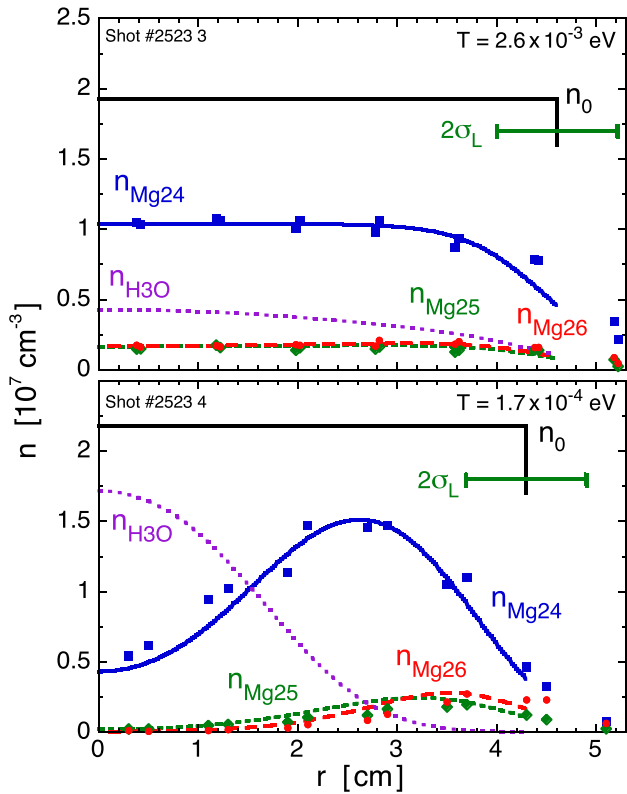
began to centrifugally separate by mass[23–26] forming distinct radial annuli as shown in Fig. 2 (Bottom). Our laser diagnostics only detect $^{24}Mg^+$ (blue squares), and the Magnesium isotopes $^{25}Mg^+$ (green diamonds) and $^{26}Mg^+$ (red circles). The curves of Fig. 2 are the theory predicted profiles for the given temperature, radius, rotation frequency, and ion composition. The hole in the Mg^+ density profile of Fig. 2 (Bottom) reflects the presence of lighter impurity H_3O^+ ions (purple curve), which are not detected with our LIF diagnostics.

The wave damping measurements are performed throughout the course of a day on the same set of ions. Laser cooling of the $^{24}Mg^+$ enables temperature control and therefore damping measurements spanning a range in temperature from 10^{-4} to 1 eV. Typically, a new plasma is held for a few hours at a low temperature $T \sim 10^{-3}$ eV until the species reach a chemical equilibrium. After this period, the concentration of impurities remains relatively constant over the course of the damping measurements.

III. PLASMA ION COMPOSITION

The ion composition of these plasmas is determined through Thermal Cyclotron Spectroscopy (TCS).[27] Ion species are identified by an increase in the cooling fluorescence, resulting from plasma heating, when an applied RF burst is resonant with the cyclotron frequency of a species. The inset of Fig. 3 shows a schematic of this TCS process. Long RF bursts (10^4 cycles) produce narrow resonances, and are initially used to detect the ion species. A broad TCS scan showing a typical "dirty" plasma composition is shown in Fig. 3. As expected, the plasma consists of $^{24}Mg^+$, and isotopes $^{25}Mg^+$ and $^{26}Mg^+$; impurity species H_3O^+ and O_2^+ are also observed.

A quantitative determination of the species charge fraction δ_s is then obtained by measuring the resulting heating from short, resonant cyclotron bursts (200–800 cycles). These short cyclotron bursts cause a change in the plasma temperature
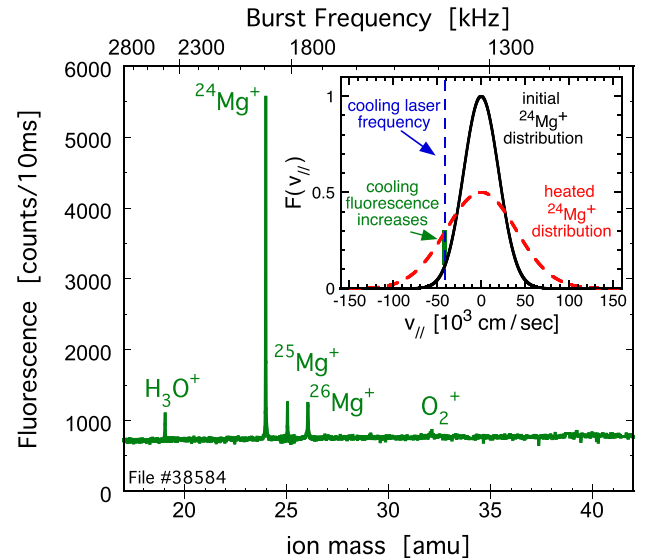

FIG. 2. Measured Mg^+ density (symbols) of a typical "dirty" plasma for both a warm, radially uniform (Top), and a cold, centrifugally separated (Bottom) profile. Curves are theory predicted profiles for the given plasma radius, rotation frequency, ion composition, and temperature; convolved by the width of the laser beam $\sigma_L \sim 0.6$ cm. At these low temperatures, the total charge density profile (solid black) is a "top-hat," with density n_0 measured through the E × B rotation frequency.

FIG. 3. Mass spectrum of a typical "dirty" plasma. A 10^4 cycle, 0.6 V$_{pp}$ RF burst heats the plasma when resonant with the cyclotron frequency of a species, which produces a change in the cooling fluorescence (inset).

$\Delta T_s \propto (\delta_s/M_s)(A_s \tau_s)^2$, where M_s is the species mass, A_s is the burst amplitude, and τ_s is the burst period.[26] Here, we vary the burst amplitude and period applied to each species to produce a consistent change in the plasma temperature, inferred from equivalent changes in the cooling fluorescence. The relative charge fraction of two species is then $\delta_s/\delta_{s'} = (M_s/M_{s'})(A_{s'}/A_s)^2(\tau_{s'}/\tau_s)^2$.

To convert from relative to individual charge fractions, we either measure the charge fraction of $^{24}Mg^+$ from the frequency shift of the cyclotron modes,[26] or assume the measured $\Sigma \delta_s = 1$; both methods give nearly identical results. The individual charge fractions are measured to a 10% accuracy down to a $\delta_s \sim 0.5\%$ level. A typical "dirty" plasma composition consists of the three naturally occurring Magnesium isotopes (24, 25, and 26), H_3O^+ (19), HCO^+ (29), O_2^+ (32), $C_3H_3^+$ (39), and $C_3H_7^+$ (43); with $\delta_s \sim (52, 9, 10, 16, 4, 4, 4, 1)\%$, respectively.

IV. PLASMA WAVE DAMPING

These damping measurements are performed on azimuthally symmetric, standing plasma waves. In these trapped plasmas, the dispersion relation of these waves is near-acoustic because of the shielding of the cylindrical confinement electrodes at a radius $R_w = 2.86$ cm. This Trivelpiece-Gould (TG) dispersion relation[28] for azimuthally symmetric modes is

$$f_{TG} = f_p \frac{k_z}{\sqrt{k_z^2 + k_\perp^2}} \left[1 + \frac{3}{2} \left(\frac{\bar{v}}{v_{ph}} \right)^2 \right], \quad (1)$$

where $k_z \equiv m_z \pi / L_p$ and $k_\perp \sim R_p^{-1}[2/\ln(R_w/R_p)]^{1/2}$ are the axial and transverse wavenumbers, respectively, and f_p is the plasma frequency. For most of this work, we investigate the damping of the lowest order $m_z = 1$ axial mode occurring at a frequency $f_1 \sim 26$ kHz, with phase velocity $v_{ph} = 5200$ m/s compared to thermal velocity $\bar{v} = 63$ m/s at $T = 10^{-3}$ eV.

To excite these plasma waves, a 10 cycle sine wave burst near the mode frequency is applied to the end ring shown in Fig. 1. Typically, a 5 mV$_{pp}$ amplitude is used, which creates a wave density perturbation $\delta n/n_0 \sim 0.5\%$, and wave fluid velocity $v_f \sim 20$ m/s. These small amplitude bursts generally heat the plasma by approximately 3×10^{-5} eV.

Figure 4 (Top) shows the resulting wave detected as induced image charge on a confinement ring located slightly off of the plasma center. This image charge induced voltage is digitized at a sample rate of 1 MHz, and is directly related to the wave density perturbation through Gauss's Law by

$$\frac{\delta n}{n_0} = \left[\frac{(k_z^2 + k_\perp^2)k_z C \mathcal{S}(k_z, R_p, R_w)}{2\pi e n_0 J_0(k_\perp R_p)\hat{f}} \right] V_w. \quad (2)$$

Here, C is the capacitance of the detection ring extending axially from position z_1 to z_2, $\hat{f} = \sin(k_z z_2) - \sin(k_z z_1)$ is the finite overlap of the detection ring and plasma wave, and $\mathcal{S}(k_z, R_p, R_w) = I_0(k_z R_p)K_0(k_z R_w) - I_0(k_z R_w)K_0(k_z R_p)$ relates the radial electric field at the wall to the axial electric field in the plasma. Equation (2) reduces to that of Ref. 29 for long,
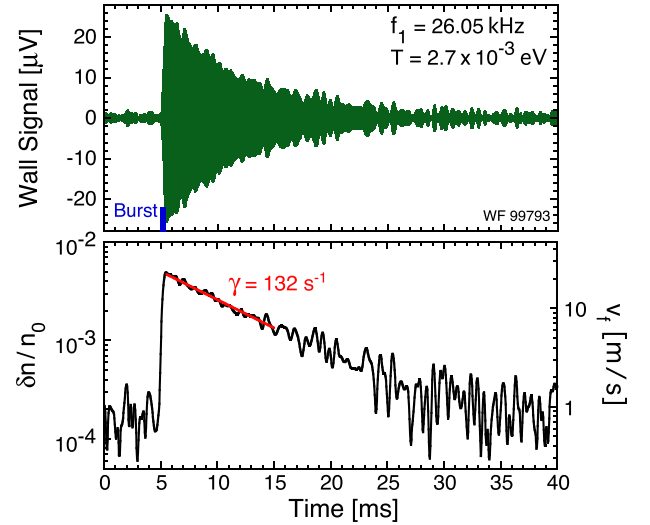

FIG. 4. Digitized wall signal (Top) of an $m_z = 1$ TG wave, and the resulting amplitude evolution (Bottom). An exponential fit (red curve) to the decreasing amplitude determines the damping rate. The measured mode frequency remains constant over the evolution.

thin plasmas, but increases $\delta n/n_0$ by about 5%–20% for the typical plasmas in these experiments.

To obtain the damping rate γ of these waves, the digitized wall signal is first fit with a sine wave in time segments of approximately 5 wave cycles. Figure 4 (Bottom) shows the resulting evolution of the wave amplitude. An exponential fit (red line of Fig. 4) to this decreasing wave amplitude then determines the damping rate. At $T = 2.7 \times 10^{-3}$ eV, a typical damping rate is $\gamma \sim 132$ s^{-1} for a "dirty" plasma composition.

By changing the strength of the laser cooling, the damping rate of these plasma waves is measured over four decades in the plasma temperature $10^{-4} \lesssim T \lesssim 1$ eV. At high temperatures $T \gtrsim 0.2$ eV, thermal particles are near the wave phase velocity, and collisionless Landau damping dominates[20] with linear Landau rates $50 \lesssim \gamma_L \lesssim 8000$ s^{-1}. In the temperature range $0.02 \lesssim T \lesssim 0.2$ eV, prior experiments suggest that the wave damping is dominated by bounce harmonic Landau damping introduced through finite-length effects.[30]

The experiments reported here focus on $T \lesssim 10^{-2}$ eV, where the damping is dependent on the plasma composition and scales roughly as $T^{-3/2}$. Shown in Fig. 5 are damping measurements on plasmas with three different compositions. As the concentration of impurities is increased from the "clean" to "dirty" plasma, we find that the damping increases by a factor of 4. At temperatures below $T \sim 10^{-3}$ eV, the damping is observed to decrease from the $T^{-3/2}$ scaling, consistent with the onset of centrifugal mass separation and collisional locking of the fluid elements.

For a given composition, the scatter of the different symbol shapes corresponds to damping measurements on different plasmas with slight compositional variations, but roughly the same damping. The uncertainty in the measured damping rates is about ±10%, which is smaller than the vertical size of the symbols. The horizontal error bars reflect the degree of non-uniformity in the radial plasma temperature; symbols are plotted at the average radial temperature.
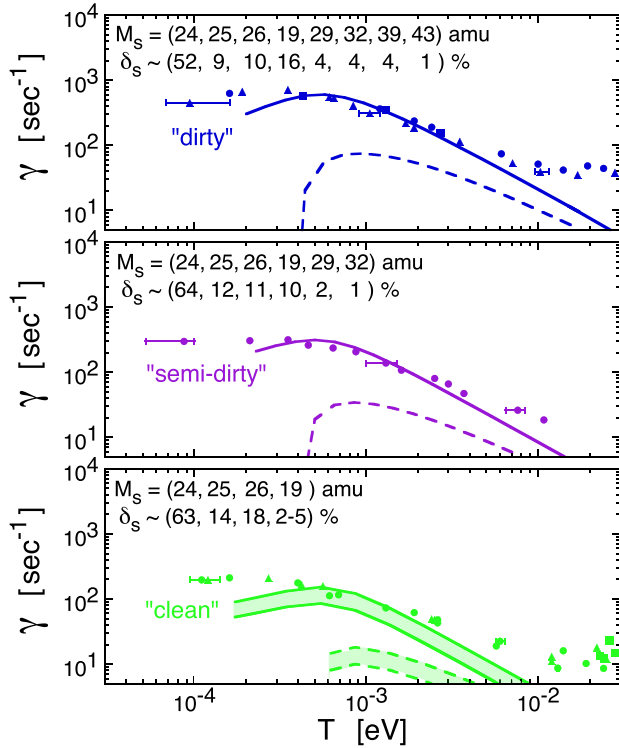
FIG. 5. Measurements (symbols) of interspecies collisional drag damping on plasmas with three different species compositions and a density $n_0 \sim 1.9 \times 10^7$ cm^{-3}. Symbol shapes represent measurements on different plasmas. Curves correspond to drag damping predictions for both a classical calculation that assumes only short-range collisions (dashed), and a calculation including the new long-range enhanced collisional slowing (solid).

V. INTERSPECIES DRAG

The characteristic $T^{-3/2}$ collisional scaling of the damping measurements and their dependence on the plasma composition suggest interspecies collisional drag as the damping mechanism. Basically, ions are accelerated by the wave electric field as $q_s E/M_s$ producing a disparity in the velocity of different species. Collisions between species then produce drag forces, which damps the wave. Cold fluid theory predicts the oscillating velocity $v_f^{(s)}$ of species s parallel to the magnetic field to be

$$v_f^{(s)} = \frac{q_s k_z \delta\phi}{M_s \omega} - i \sum_{s'} \frac{\nu_{ss'}}{\omega} \left(v_f^{(s)} - v_f^{(s')} \right), \qquad (3)$$

where $\nu_{ss'}$ is the collisional slowing rate between species s and s', $\delta\phi$ is the wave potential, and ω is the complex wave frequency. In the limit of weak collisionality ($\nu_{ss'} < \omega$), the measured wave induced fluid velocity of each of the Mg$^+$ isotopes[20] is consistent with Eq. (3).

For $T \gtrsim 10^{-3}$, these plasmas are radially uniform and have weak collisionality ($\nu_{ss'} < \omega$). In this regime, the drag damping can be solved analytically as

$$\gamma = \frac{1}{4\omega_p^2} \sum_s \sum_{s'} \frac{(M_{s'} - M_s)^2}{M_{s'}^2} \omega_{p,s}^2 \nu_{ss'}, \qquad (4)$$

where $\omega_{p,s}^2 = 4\pi q_s^2 n_s / M_s$ is the species plasma frequency, and $\omega_p^2 = \Sigma \omega_{p,s}^2$ is the total plasma frequency. Equation (4)

recovers the electron-ion drag damping results of Lenard and Bernstein[31] for neutral plasmas.

In contrast, for $T \lesssim 10^{-3}$, the species began to centrifugally separate by mass, and the species fluid elements began to collisionally lock ($\nu_{ss'} \sim \omega$). The drag damping in this regime is calculated by solving for $\omega \equiv \omega_r + i\gamma$ in the linearized Poisson equation

$$\frac{1}{r}\frac{\partial}{\partial r}\left(r\frac{\partial \delta\phi}{\partial r} \right) - k_z^2 \delta\phi = -\frac{4\pi q_s k_z}{\omega} \sum_s n_s v_f^{(s)}, \qquad (5)$$

using a shooting method. Here, the linearized continuity equation $\delta n_s = k_z n_s v_f^{(s)}/\omega$ has been used to replace the perturbed density δn_s with the species velocity $v_f^{(s)}$. The species velocity is obtained in terms of $\delta\phi(r)$ by solving Eq. (3) for general ω. The collision rate $\nu_{ss'}$ is obtained from theory (see Sec. VI) for a given equilibrium density, temperature, and species fraction.

Some insight into how centrifugal separation and fluid locking affect the drag damping is obtained by considering a multispecies plasma in which a single species is dominate. For such a plasma, the collisions on the minority species α are negligible compared to the collisions on the single majority species β, so the $\nu_{\beta\alpha}$ terms can be neglected in the analysis. In this limit, the drag damping can be solved analytically as

$$\gamma = \frac{\frac{1}{2}\sum_\alpha \int rdr |\delta\phi|^2 \frac{(M_\beta - M_\alpha)^2}{M_\beta^2} \frac{1}{1 + (\nu_{\alpha\beta}/\omega)^2} \omega_{p,\alpha}^2 \nu_{\alpha\beta}}{\int rdr |\delta\phi|^2 \omega_p^2}, \qquad (6)$$

including the effects of centrifugal separation and fluid locking. This analysis shows that the drag damping is reduced from the prediction of Eq. (4) when the collision rate approaches the wave frequency, and the species began to collisional lock. The damping is also reduced as the species centrifugally separate by mass. Equation (6) involves a radial integral over $\omega_{p,\alpha}^2 \nu_{\alpha\beta} \propto n_\alpha(r) n_\beta(r)$, so the drag damping is decreased as the radial overlap between the species is reduced.

VI. PARALLEL COLLISIONAL SLOWING

Recent parallel collision theory[17] resolves inconsistencies between Fokker-Planck[18] and Boltzmann[19] analysis of long-range frictional drag by introducing a novel but fundamental length scale

$$d \equiv \left[\frac{(e^2/\mu)^3}{(D_s + D_{s'})^2} \right]^{1/5} \propto T^{1/5}, \qquad (7)$$

where $\mu = M_s M_{s'}/(M_s + M_{s'})$ is the reduced mass, and $D_s = \Sigma \nu_{ss'} T/M_s$ is parallel velocity diffusion coefficients for species s. This new scale length divides long-range collisions into separate regimes depending on the timescale of the collision. When two particles with guiding centers on different field lines separated by a distance $\rho > r_c$ approach one another, a collision that affects the slowing rate (a reflection) occurs only if the initial relative kinetic energy $\mu |v_\parallel^{(s)} - v_\parallel^{(s')}|^2/2$ is less

than the Coulomb potential energy $q_s q_{s'}/\rho$. This sets a time-scale $t_B \equiv \rho(|q_s q_{s'}|/\mu\rho)^{-1/2}$ for an affective Boltzmann collision. For close particles $\rho < d$, the collisions occur faster than the diffusion timescale, so they can be regarded as isolated Boltzmann collisions. In contrast, for well-separated particles $\rho > d$, the Boltzmann collision timescale is longer than the diffusion timescale, so multiple weak collisions occur simultaneously and particles diffuse in velocity. In this regime, Fokker-Planck theory is required.

Therefore, the slowing down rate must be derived separately for each regime, and the results only applied to the relevant range of impact parameters. This theory[17] predicts that the slowing-down rate has the "classical" collisional scaling

$$\nu_{ss'} = \sqrt{\pi} n_{s'} \bar{v}_{ss'} b^2 \ln\Lambda, \qquad (8)$$

where $\bar{v}_{ss'} \equiv \sqrt{2T\mu}/M_s$, but that the collision rate is enhanced by a new Coulomb logarithm

$$\ln\Lambda = \frac{4}{3}\ln\left(\frac{\min[r_c, \lambda_D]}{b}\right) + h\ln\left(\frac{d}{\max[b, r_c]}\right) + 2\ln\left(\frac{\lambda_D}{\max[d, r_c]}\right). \qquad (9)$$

In Eq. (9), the first logarithmic term is from classical short-range collisions, and is equivalent to $5\nu_{ii}/4$.[32] The second and third terms represent an enhancement in the collisional slowing rate resulting from long-range Boltzmann and Fokker-Planck collisions, respectively. For attractive (opposite-sign) collisions in neutralized plasmas, no reflection of the guiding centers occurs, and the long-range Boltzmann collision rate vanishes $h = 0$, whereas, for the repulsive (like-sign) collisions present in these experiments $h = 5.899$, increased from 4 due to "collisional caging."[11]

In Fig. 6, these short and long-range collision rates are plotted over a range in temperature for our typical "dirty" plasma. Long-range, 1D Boltzmann collisions (red curve) clearly dominate the collisionality in these plasmas, exceeding the classical short-range collision rate (blue curve) by as much as an order of magnitude. At low temperatures $T < 4 \times 10^{-4}$ eV, the plasma becomes strongly magnetized (i.e.,
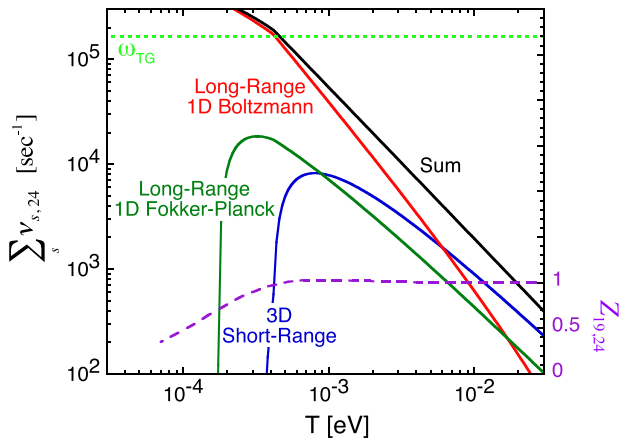

FIG. 6. Short and long-range collision rates versus temperature for a typical "dirty" plasma. The purple dashed line is the radial overlap between species $^{24}Mg^+$ and H_3O^+ [see Eq. (10)], and the green dashed line is the $m_z = 1$ mode frequency.

$r_c < b$), and the short-range collision rate approaches zero because the cyclotron energy of the colliding pairs is an adiabatic invariant.[33] Long-range, 1D Fokker-Planck collisions (green curve) are rather weak by comparison for this density and range of temperatures, and approach zero for $T \lesssim 2 \times 10^{-4}$ eV when $\lambda_D < d$.

This long-range enhancement of the parallel collision rate should cause stronger interspecies collisional drag damping, and that is exactly what we observe. Figure 5 shows drag damping predictions for both a classical calculation that assumes only short-range collisions (dashed curve), and a calculation including the new long-range enhanced collisional slowing (solid curve). The theory is in quantitative agreement with the experiments only when long-range collisions are included, exceeding short-range collision predictions by as much as an order of magnitude. The larger uncertainty in the "clean" plasma species composition results in a broader theory curve.

Around $T \sim 10^{-2}$ eV, the measured damping rates are larger than the drag damping predictions. This discrepancy may be a result of another damping mechanism. Cold fluid theory predicts that these TG waves are also damped from viscous momentum transfer along and across the magnetic field.[34] In this temperature regime, this damping is too weak ($\gamma \sim 5$ s^{-1}) to explain the discrepancy we observe, but an enhancement of this damping is predicted from finite-length effects.[35] Bounce harmonic Landau[30] damping is another mechanism that may increase the damping in this temperature regime.

VII. CENTRIFUGAL SEPARATION AND FLUID LOCKING

In this section, we investigate two effects, which occur at $T \lesssim 10^{-3}$ eV, that reduce the drag damping from the collisional $T^{-3/2}$ scaling. First, the ions begin to centrifugally separate by mass, with the lighter ions near $r = 0$, as shown in Fig. 2 (Bottom). The dashed purple curve of Fig. 6 represents the radial overlap between species $s = {}^{24}Mg^+$ and $s' = H_3O^+$, defined as

$$Z_{ss'} \equiv \frac{2\int_0^{R_p} \hat{\delta}_s(r)\hat{\delta}_{s'}(r) r\, dr}{\delta_s \delta_{s'} R_p^2}, \qquad (10)$$

where $\hat{\delta}_s(r)$ is the relative concentration of species s at radius r, and δ_s is the total fraction of species s. On warm plasmas $T \gtrsim 10^{-3}$ eV, the species are radially uniform and $Z_{ss'} = 1$. However, as the species centrifugally separate, $Z_{ss'}$ decreases, approaching zero for complete radial separation. This reduction in the radial species overlap decreases the interspecies drag damping from the $T^{-3/2}$ scaling. Of course, $Z_{ss'}$ represents radially local collisions only, and non-local interactions will persist even with complete radial separation, but non-local interaction are not included in the current theory. These non-local interaction, which would appear as viscous terms in Eq. (3), may explain the discrepancy between the measured and predicted damping rates at ultra-low temperatures $T \lesssim 4 \times 10^{-4}$ eV.

The second effect that reduces the drag damping from the collisional scaling is collisional locking of the species. When the collisionality approaches the wave frequency ω (green dashed line in Fig. 6) around $T \sim 10^{-3}$ eV, the species collide before developing a disparity in velocity. In essence, the species fluid elements begin to collisionally lock, which decreases the drag.

These two effects are dependent on the density of the plasma. At higher densities, the plasma $E \times B$ rotates at a faster rate, and therefore centrifugal separation occurs at a higher temperature. Also, the ratio $\nu_{ss'}/\omega$ increases with the plasma density, so fluid locking will also occur at higher temperatures.

Figure 7 shows drag damping measurements on two different density plasmas. First, these data points show a similar quantitative agreement with long-range enhanced drag damping theory as the plasma density is changed by a factor of 7. Next, we see that at high densities, where the effects of centrifugal separation and fluid locking are more prominent, the maximum damping rate occurs at higher temperatures. These results suggest that fluid locking and centrifugal separation are at least in part responsible for the decrease in the damping from the $T^{-3/2}$ scaling.

To isolate how reducing the radial overlap between the species influences the drag damping, we use the fact that the plasma thermally equilibrates on a faster timescale than the species diffuse radially. This enables, for a short period of time, the creation of a warm plasma with a reduced $Z_{ss'}$. Figure 8 depicts the details of this process. The plasma is initially cooled to a low temperature $T \sim 10^{-4}$ eV, where the species are centrifugally separated by mass. At $r = 0.3$ cm on a $R_p = 0.5$ cm plasma, Fig. 8(a) shows the measured ^{25}Mg$^+$ and ^{26}Mg$^+$ peaks (blue) as $2\times$ and $4\times$ smaller than expected for a uniform profile (red dashed curves). Then, at 20 ms, the plasma is abruptly heated by wiggling the plasma end with a 500 mV$_{pp}$, 200 cycle burst at 36 kHz. The plasma temperature is shown in Fig. 8(c) to re-equilibrate after this heating burst
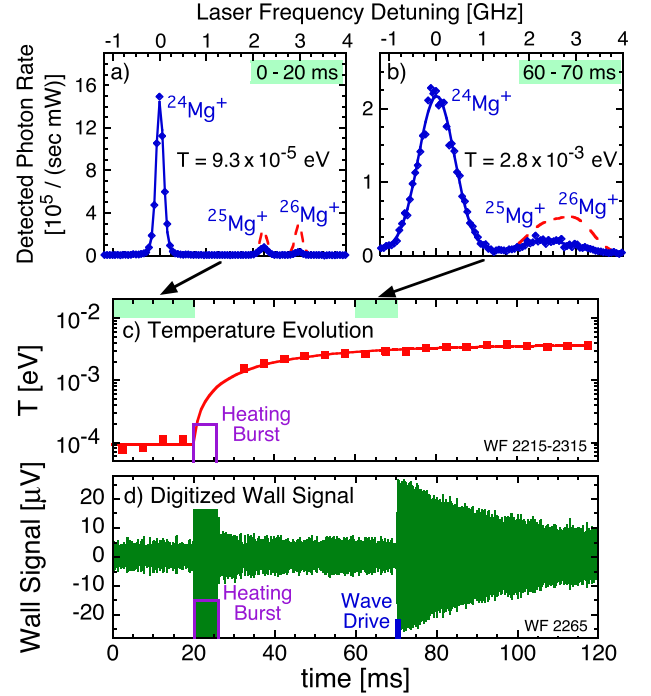
FIG. 8. Process for creating a warm plasma with reduced radial overlap between the species. The blue curves of (a) and (b) are the measured Mg$^+$ distributions at a radius of 0.3 cm before and after a heating burst, respectively, and the red dashed curves are what the distributions would look like on a radially uniform plasma. The plasma temperature equilibrates (c) before the species have remixed, enabling damping measurements (d) on a warm but radially non-uniform plasma.

to $T \sim 3 \times 10^{-3}$ eV on a 20 ms timescale. But, on this timescale, the species have not remixed radially [Fig. 8(b)]. The species generally remix on a diffusion timescale of about 500 ms. By exciting a wave before the species have remixed [Fig. 8(d)], we are able to measure the drag damping on a warm plasma with a reduced radial species overlap. This process can be repeated for different heating burst amplitudes to change the plasma temperature and hence collisionality, while keeping the species overlap $Z_{ss'}$ roughly constant.

Figure 9 shows damping measurements on a typical "dirty" plasma for which the overlap integral $Z_{19,24}(T)$ results from the standard temperature dependent centrifugal separation, and on the same "dirty" plasma for which the radial species overlap is kept small and constant at $Z_{19,24} \sim 0.43$ determined by the initial $T \sim 10^{-4}$ eV equilibrium profile. Clearly, reducing the species overlap reduces the drag damping. At $T \sim 2 \times 10^{-3}$ eV, $Z_{19,24}$ differs from 1 to 0.43, and the damping rate is reduced by a factor of 4. The agreement between theory and experiments for $T \gtrsim 6 \times 10^{-4}$ eV demonstrates that the influence of centrifugal separation is properly modeled by radially local collisions in this temperature regime. The data for $T < 6 \times 10^{-4}$ eV are inconclusive. In this ultra-low temperature regime, viscous effects may be important, which are neglected in the current theory analysis.

The effect that collisional locking of the species fluid elements has on the drag damping is investigated by measuring the damping rate of higher frequency axial modes, with frequency $f_1 = 27.25$ kHz, $f_2 = 50.35$ kHz, and $f_3 = 68.45$ kHz. This interspecies drag damping depends on the disparity in
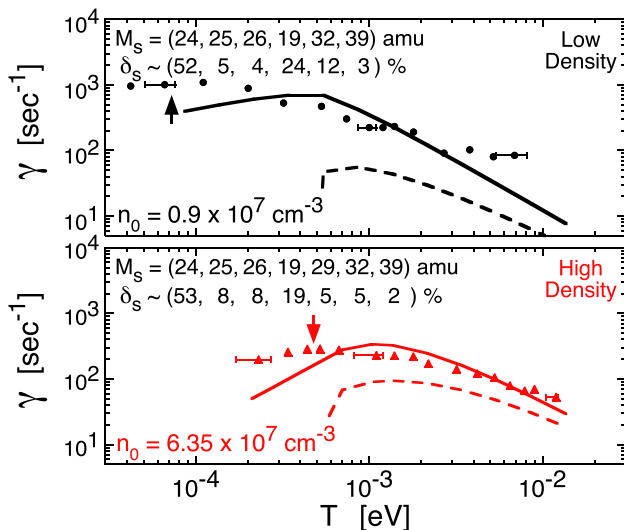

FIG. 7. Drag damping measurements (symbols) for two different density plasmas with different compositions. Curves are theory predictions assuming either classical collisions (dashed) or long-range enhanced collisions (solid). Arrows indicate the temperature at which the maximum measured damping is reached.
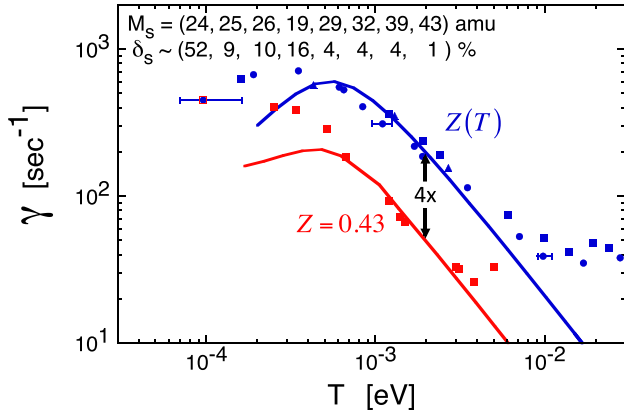
FIG. 9. Blue symbols and curve are the standard measurements and theory prediction of drag damping on a typical "dirty" plasma with radial species overlap $Z(T)$ due to centrifugal separation. In contrast, the red symbols and curve represent damping measurements on the same "dirty" plasma composition, but with a constant, reduced radial species overlap $Z_{19,24} \sim 0.43$ determined by the initial $T \sim 10^{-4}$ eV equilibrium profile.

the velocity between the species, and not on the axial mode structure, so higher frequency axial modes are predicted to have the same damping rate in the weak collisionality regime. However, collisional locking becomes important when the collisionality approaches the wave frequency, as shown by the $\nu_{\alpha\beta}/\omega$ term in Eq. (6), so the higher frequency modes will have less fluid locking for a given temperature.

Figure 10 shows the damping rate of the first three axial modes ($m_z = 1$, 2, and 3). For $T \gtrsim 3 \times 10^{-4}$ eV, the higher frequency modes are all damped at the same rate, as predicted by theory in the weak collisionality regime. In contrast, below $T \lesssim 3 \times 10^{-4}$ eV, the higher frequency modes are more heavily damped, which suggests less fluid locking. This stronger damping is in qualitative agreement with theory, which predicts about a factor of 2 increase in the damping rate for $m_z = 3$ at $T = 3 \times 10^{-4}$ eV.

In general, these TG waves are more heavily damped than the current theory prediction at ultra-low temperatures $T \lesssim 4 \times 10^{-4}$ eV. In this centrifugally separated temperature regime, nonlocal interaction may be significant, which are not included in the current theory. Also, for the typical

density $n_0 = 1.9 \times 10^7$, the plasma ions becomes moderately correlated, with correlation parameter $\Gamma \equiv e^2/aT \gtrsim 0.2$ for $T \lesssim 4 \times 10^{-4}$ eV, where $a = (3/4\pi n_0)^{1/3}$ is the Wigner-Seitz radius. Correlations may limit the parallel collisionality,[36,37] decreasing the effects of fluid locking and increasing the predicted damping rates.

VIII. CONCLUSION

When Landau damping is weak ($T \lesssim 10^{-2}$ eV), the damping of axial plasma waves in magnetized, multispecies ion plasmas is dominated by interspecies collisional drag. This drag damping is in quantitative agreement with theory only when long-range collisions are included, exceeding classical predictions by as much as an order of magnitude. At temperatures below $T \sim 10^{-3}$ eV, the damping decreases from the $T^{-3/2}$ collisional scaling. Damping measurements in plasmas with a non-equilibrium species profile and of higher frequency axial modes showed that centrifugal mass separation and collisional locking of the species, which occur at these low temperatures, are at least in part responsible for this decreased damping.
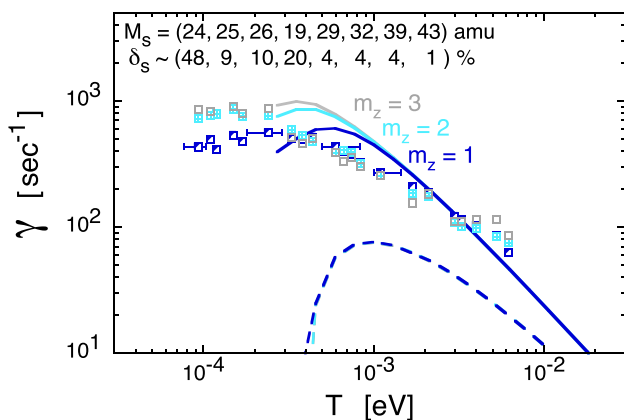
FIG. 10. Drag damping measurements of higher frequency axial modes with $f_1 = 27.25$ kHz, $f_2 = 50.35$ kHz, and $f_3 = 68.45$ kHz. Dashed lines are theory curves assuming classical collisions and solid curves are the same theory assuming long-range enhanced collisions.

[1]L. Spitzer and R. Härm, Phys. Rev. **89**, 977 (1953); R. S. Cohen, L. Spitzer, and P. M. Routly, *ibid.* **80**, 230 (1950).
[2]C. L. Longmire and M. N. Rosenbluth, Phys. Rev. **103**, 507 (1956).
[3]M. N. Rosenbluth and A. N. Kaufman, Phys. Rev. **109**, 1 (1958).
[4]J. A. Boedo, D. L. Rudakov, R. A. Moyer, G. R. McKee, R. J. Colchin, M. J. Schaffer, P. Stangeby, W. West, S. L. Allen, T. E. Evans *et al.*, Phys. Plasmas **10**, 1670 (2003).
[5]Y. Liang, H. Koslowski, P. Thomas, E. Nardon, B. Alper, P. Andrew, Y. Andrew, G. Arnoux, Y. Baranov, M. Bécoulet *et al.*, Phys. Rev. Lett. **98**, 265004 (2007).
[6]B. LaBombard, J. Rice, A. Hubbard, J. Hughes, M. Greenwald, J. Irby, Y. Lin, B. Lipschultz, E. Marmar, C. Pitcher *et al.*, Nucl. Fusion **44**, 1047 (2004).
[7]A. M. Beloborodov and C. Thompson, Astrophys. J. **657**, 967 (2007).
[8]G. Andresen, M. Ashkezari, M. Baquero-Ruiz, W. Bertsche, P. D. Bowe, E. Butler, C. Cesar, S. Chapman, M. Charlton, A. Deller *et al.*, Nature **468**, 673 (2010).
[9]G. Gabrielse, X. Fei, L. A. Orozco, R. L. Tjoelker, J. Haas, H. Kalinowsky, T. A. Trainor, and W. Kells, Phys. Rev. Lett. **63**, 1360 (1989).
[10]B. M. Jelenković, A. S. Newbury, J. J. Bollinger, W. M. Itano, and T. B. Mitchell, Phys. Rev. A **67**, 063406 (2003).
[11]D. H. E. Dubin, Phys. Rev. Lett. **79**, 2678 (1997).
[12]F. Anderegg, X.-P. Huang, C. F. Driscoll, E. M. Hollmann, T. M. O'Neil, and D. H. E. Dubin, Phys. Rev. Lett. **78**, 2128 (1997).
[13]D. H. E. Dubin and T. O'Neil, Phys. Rev. Lett. **78**, 3868 (1997).
[14]E. Hollmann, F. Anderegg, and C. Driscoll, Phys. Rev. Lett. **82**, 4839 (1999).
[15]C. Driscoll, J. Malmberg, and K. Fine, Phys. Rev. Lett. **60**, 1290 (1988).
[16]J. Kriesel and C. Driscoll, Phys. Rev. Lett. **87**, 135003 (2001).
[17]D. H. E. Dubin, Phys. Plasmas **21**, 052108 (2014).
[18]N. Rostoker, Phys. Fluids **3**, 922 (1960).
[19]T. M. O'Neil, Phys. Fluids **26**, 2128 (1983).
[20]M. Affolter, F. Anderegg, D. H. E. Dubin, and C. F. Driscoll, Phys. Rev. Lett. **117**, 155001 (2016).
[21]F. Anderegg, X.-P. Huang, E. Sarid, and C. Driscoll, Rev. Sci. Instrum. **68**, 2367 (1997).
[22]F. Anderegg, E. Hollmann, and C. Driscoll, Phys. Rev. Lett. **81**, 4875 (1998).
[23]T. O'Neil, Phys. Fluids **24**, 1447 (1981).

[24]G. B. Andresen, M. D. Ashkezari, M. Baquero-Ruiz, W. Bertsche, P. D. Bowe, E. Butler, C. L. Cesar, S. Chapman, M. Charlton, A. Deller, S. Eriksson, J. Fajans, T. Friesen, M. C. Fujiwara, D. R. Gill, A. Gutierrez, J. S. Hangst, W. N. Hardy, M. E. Hayden, A. J. Humphries, R. Hydomako, S. Jonsell, N. Madsen, S. Menary, P. Nolan, A. Olin, A. Povilus, P. Pusa, F. Robicheaux, E. Sarid, D. M. Silveira, C. So, J. W. Storey, R. I. Thompson, D. P. van der Werf, J. S. Wurtele, and Y. Yamazaki, Phys. Rev. Lett. **106**, 145001 (2011).

[25]D. Larson, J. Bergquist, J. Bollinger, W. M. Itano, and D. Wineland, Phys. Rev. Lett. **57**, 70 (1986).

[26]M. Affolter, F. Anderegg, D. H. E. Dubin, and C. Driscoll, Phys. Plasmas **22**, 055701 (2015).

[27]M. Affolter, F. Anderegg, D. H. E. Dubin, and C. Driscoll, Phys. Lett. A **378**, 2406 (2014).

[28]A. Trivelpiece and R. Gould, J. Appl. Phys. **30**, 1784 (1959).

[29]J. Danielson, F. Anderegg, and C. Driscoll, Phys. Rev. Lett. **92**, 245003 (2004).

[30]F. Anderegg, M. Affolter, A. A. Kabantsev, D. H. E. Dubin, A. Ashourvan, and C. F. Driscoll, Phys. Plasmas **23**, 055706 (2016).

[31]A. Lenard and I. B. Bernstein, Phys. Rev. **112**, 1456 (1958).

[32]T. M. ONeil and C. F. Driscoll, Phys. Fluids **22**, 266 (1979).

[33]M. E. Glinsky, T. M. ONeil, M. N. Rosenbluth, K. Tsuruta, and S. Ichimaru, Phys. Fluids B **4**, 1156 (1992).

[34]M. Anderson and T. ONeil, Phys. Plasmas **14**, 112110 (2007).

[35]M. Anderson, T. ONeil, D. H. E. Dubin, and R. Gould, Phys. Plasmas **18**, 102113 (2011).

[36]G. Dimonte and J. Daligault, Phys. Rev. Lett. **101**, 135001 (2008).

[37]S. D. Baalrud and J. Daligault, Phys. Rev. Lett. **110**, 235001 (2013).